THE ASTRONOMICAL JOURNAL VOLUME 107, NUMBER 3 MARCH 1994

KINEMATICS OF 12 ELLIPTICAL GALAXIES

JOSEF W. FRIED
Max-Planck-Institut fur Astronomie, Königstuhl, D-69117 Heidelberg 1, Germany
Electronic mail: fried@mpia-hd.mpg.de

GARTH D. ILLINGWORTH[1]
UCO/Lick Observatory, University of California, Santa Cruz, California 95064
Electronic mail: gdi@surya.ucsc.edu

Received 1993 October 28

ABSTRACT

Long-slit spectroscopic data for a sample of 12 elliptical galaxies have been analyzed to derive velocity dispersion and rotational velocity profiles. Minor axis profiles are also given for two galaxies, NGC 2768 and IC 1459. These data clearly demonstrate the large range of rotational properties known to exist in luminous elliptical galaxies ($M_B \leqslant -20$ for $H_0 = 50$ km s^{-1} Mpc^{-1}). The spectroscopic data typically have quite high S/N and can be used to derive velocity dispersion and rotation velocity profiles out to radii $r \sim r_e$. The mean logarithmic gradient of the velocity dispersion profiles is small; σ decreases by only 20% for an order of magnitude change in radius from $\sim 0.1 r_e$ to $\sim r_e$. The ellipticals in this sample are also found to have a very small range in their logarithmic gradients. Even though rotation is energetically unimportant, the rotation curves in ellipticals are typically "flat" at radii larger than $0.2 r_e$, and often at radii beyond $0.1 r_e$. A spectrum offset from the nucleus of the E6/S0 galaxy NGC 2768 is used to characterize the form of the velocity distribution in this quite flattened galaxy (it decreases rapidly with z). Observations of the gas (from O[II]) show that there exists a polar gas disk in the inner regions of NGC 2768.

1. INTRODUCTION

The low mean rotation (in a dimensionless v_m/σ sense) and the large dispersion in rotational properties of elliptical galaxies are well known effects. Binney (1978) suggested that elliptical galaxies are triaxial. Since then our view has developed to where they are now generally considered to be triaxial objects (see, e.g., Franx *et al.* 1991), whose figures arise through anisotropy in the stellar velocity distribution. Net streaming (rotation) does appear, however, to be a common feature of elliptical galaxies. Franx *et al.* (1989b, hereafter referred to as FIH) found that only one of 22 ellipticals appeared to have no measurable rotation (where $v_{\rm rot} < 20$ km s^{-1} on both the major and minor axes).

Amongst the many characteristics of elliptical galaxies that remain poorly defined is the form of the rotation and velocity dispersion profiles. Because of the difficulty of obtaining high S/N data, much of the available data is inadequate for determining, for example, the gradients in the velocity dispersion profiles. The new data presented here, even though taken using an image intensifier and photographic plates, are often of higher quality than most previously available data—primarily because of the longer integrations needed to give a measurable photographic density, at which level the S/N on IIIa-J emulsions is quite high. Long-slit spectroscopic observations of 12 elliptical galaxies have been analyzed to provide rotational velocity and velocity dispersion profiles out to large radii; $r \sim r_e$ in many cases. Not many ellipticals have kinematic data that approach such radii.

2. OBSERVATIONAL DATA

The program objects were drawn from a variety of catalogs, and were chosen to be the nearer and brighter elliptical galaxies ($M_B < -20$, for $H_0 = 50$ km s^{-1} Mpc^{-1}). No particular selection criteria were applied. The sample is summarized in Table 1, along with cataloged properties of the galaxies, including their radio, far-IR (IRAS 10 μm) and x-ray fluxes. These data were taken from several sources, as detailed in the notes following Table 1. No particular bias was used in their selection, except to exclude obviously dusty or unusual objects. In general, objects flatter than E2 were selected so that the major axis position angle could be ascertained from images (surface photometry of a large sample of ellipticals was not generally available at the time of the selection of this sample). This contrasts with the bias towards rounder galaxies in the sample that was selected for study by FIH.

The procedures and instrumental configurations used to acquire these photographic image intensifier observations have been described by Illingworth & Schechter (1982), Davies & Illingworth (1983) and Binney *et al.* (1990). In summary, all except one of the spectra were obtained with the CTIO and KPNO 4 m R.C. spectrographs using an RCA C33063 image intensifier and N_2-baked IIIa-J plates. The exception was a spectrum of NGC 2768 obtained with

[1]Visiting Astronomer at the Kitt Peak National Observatory and the Cerro Tololo Inter-American Observatory, operated by AURA, Inc., under contract to the National Science Foundation.

 0004-6256/94/107(3)/992/11/$0.90

TABLE 1. Observed galaxies.

Galaxy	Type RC2	Type RSA	ϵ	Θ_{ma}	σ km s^{-1}	r_e "	r_{25} "	v_{grp} km s^{-1}	B_T	M_B	F_I mJy	F_X	F_R mJy
(1)	(2)	(3)	(4)	(5)	(6)	(7)	(8)	(9)	(10)	(11)	(12)	(13)	(14)
NGC 720.....	E5/E3	E5	0.40	142	247	40	109	1728	11.16	-21.53	<170	8.64	<1
NGC 1052.....	E0/E2	E3/S0	0.27	115	206	37	102	1392	11.28	-20.94	1400	5.29	1270
NGC 2768.....	E6/E5	$S0_{1/2}(6)$	0.47	94	198	53	119	1355	10.93	-21.57	1220	...	180
NGC 3377.....	E5/E5	E6	0.47	39	131	34	104	667	11.13	-19.50	310	<2.09	<1
NGC 3557.....	E3	E3	0.25	34	292	38	95	2740	11.13	-22.56	670	...	290
NGC 4365.....	E3/E2	E3	0.24	42	248	57	144	1074	10.64	-21.02	580	2.45	<1
NGC 4406.....	E3/E3	$S0_1(3)$/E3	0.24	121	250	91	198	1074	9.87	-21.79	290	47.50	<1
NGC 4472.....	E2/E4	$E1/S0_1(1)$	0.17	159	287	104	261	1074	9.32	-22.34	<280	65.31	132
NGC 4649.....	E2/E1	$S0_1(2)$	0.18	104	341	74	203	1074	9.77	-21.89	970	31.67	20
NGC 4697.....	E6/E4	E6	0.37	67	165	75	185	1071	10.03	-21.63	1100	2.34	<1
NGC 4976.....	E4(P)	$S0_1(4)$	[a]0.30	162	170	40	111	1133	10.76	-21.02	<1060	...	<3
IC 1459.....	E3	E4	0.26	38	308	39	119	1647	10.88	-21.71	1050	3.31	887

Notes – Col. (2) and col. (3) give the classifications of the galaxies from de Vaucouleurs *et al.* (1976) (RC2) and Sandage and Tammann (1981) (RSA). The ellipticity and position angle in cols. (4) and (5) are from the surface photometry of Franx, Illingworth and Heckman (1989a), Lauer (1985), Jedrzejewski (1987 – [a]at r_e), and Peletier *et al.* (1990). The galaxy velocity dispersion and group velocity in cols. (6) and (9) are taken from Davies *et al.* (1987). Cols. (7) and (8) give the effective radius r_e and the radius r_{25} at which $\mu_B = 25$ mag arcsec^{-2}, from Burstein *et al.* (1987). The total B magnitude B_T, and the absolute magnitude M_B in cols. (10) and (11) are taken from Burstein *et al.* (1987). M_B is derived for $H_0 = 50$ km s^{-1}Mpc^{-1}. The IRAS 100μm fluxes in col. (14) are taken from Knapp *et al.* (1989), the X-ray fluxes in col. (15) are in units of 10^{13} ergs cm^{-2} s^{-1} and are taken from Canizares *et al.* (1987) and Fabbiano, Gioia and Trinchieri (1989 – for 1052), and the (typically) 5 GHz radio fluxes in col. (16) are taken from Disney and Wall (1977), Dressel and Condon (1978), Wrobel and Heeschen (1984), and Birkinshaw and Davies (1985).

the KPNO 2.1 m "Gold" spectrograph and a similar detector system. The usual calibration data and standard stellar spectra were obtained; i.e., HeNeAr full-slit arc line spectra, sensitometer spot plates, and high S/N G8-K2 III stellar spectra. The instrumental parameters used are summarized in Table 2.

The majority of the observations were made with the spectrograph slit aligned along the major axis of the galaxies. A few minor axis spectra were also obtained. In one case, NGC 2768, a spectrum was taken parallel to the minor axis, but offset by 10 arcsec along the major axis. This spectrum was used to note the way in which the rotational velocity changes with height z above the equatorial plane (see, e.g., Kormendy & Illingworth 1982; Binney *et al.* 1990).

The position angles of the major axes were derived from a variety of sources. The position angles used are tabulated in Table 3 along with the total integration times for each galaxy spectrum. In some cases, notably IC 1459, the choice of position angle was subsequently complicated by obvious rotation of the isophotes. As a result, during the course of the observational program, some spectra were taken at slightly different position angles from those originally adopted. The changes were largest for IC 1459 and

TABLE 2. Instrumental parameters.

	KPNO	CTIO
Telescope	4-m	4-m
Spectrograph[a]	RC	RC
Slit length (arcmin)	3.6	3.7
Slit width (arcsec)	1.1	1.1
Dispersion (Å mm^{-1})	49	52
Resolution – FWHM (Å)	2.6	2.8
Spatial resolution[b] – FWHM (arcsec)	~2	~1.5
Resolution[c](σ_i – km s^{-1} – "red")$^\lambda$	64	70
Resolution[c](σ_i – km s^{-1} – "blue")$^\lambda$	80	85

[λ]The spectral ranges used for the kinematic analyses were similar for the KPNO and the CTIO data, and covered "blue" (3850-4590 ÅÅ) and ("red") (4820-5650 ÅÅ) regions.
Some exceptions to the tabulated parameters apply to a small fraction of the spectra – see Table 3. [a]RCA C33063 image intensifier used with sensitized IIIa-J plates at both telescopes. [b]In typical seeing. Resolutions similar in "blue" and "red" spectra. [c]Typical values – but $\sigma_i \sim 100$ km s^{-1} for some early CTIO spectra.

TABLE 3. Observations.

Galaxy	Telescope	λ_{cent} Å	PA °	t_{int} m	slit "
(1)	(2)	(3)	(4)	(5)	(6)
NGC 720.....	CTIO 4m	5200	142	153	1.1[a]
NGC 1052.....	KPNO 4m	5200	118	40	1.1
.....	KPNO 4m	5200	118	100	1.6
.....	KPNO 4m	4200	118	90	2.0
NGC 2768.....	KPNO 4m	4200	90	[b]190	1.1
.....	KPNO 4m	4200	90	180	1.1
.....	KPNO 4m	4200	[c]0	[b]130	1.1
.....	KPNO 2m	4200	[c]0	148	2.2
NGC 3377.....	KPNO 4m	4200	37	150	1.1
.....	KPNO 4m	5200	35	[b]50	1.1
.....	KPNO 4m	5200	35	[b]100	1.1
.....	KPNO 4m	5200	35	[b]75	1.1
NGC 3557.....	CTIO 4m	4200	45	120	1.1
.....	CTIO 4m	5200	30	150	1.1
.....	CTIO 4m	5200	35	135	1.1
.....	CTIO 4m	5200	35	[b]60	2.7
NGC 4365.....	KPNO 4m	5200	39	100	1.1
NGC 4406.....	KPNO 4m	4200	130	127	1.1
NGC 4472.....	CTIO 4m	4200	156	125	1.1
.....	CTIO 4m	5200	156	135	1.1
.....	KPNO 4m	4200	156	125	1.1
.....	KPNO 4m	5200	156	[b]149	1.1
NGC 4649.....	KPNO 4m	5200[d]	96	[b]100	1.1
.....	KPNO 4m	4200	96	[b]60	1.1
.....	KPNO 4m	4200[d]	96	[b]100	1.1
NGC 4697.....	CTIO 4m	4200	62	155	1.1[a]
.....	CTIO 4m	4200[d]	62	[b]150	1.1[a]
.....	CTIO 4m	5200	62	[b]150	1.1[a]
.....	CTIO 4m	5200	62	150	1.1
.....	CTIO 4m	5200	64	150	1.1
NGC 4976.....	CTIO 4m	5200	[e]165	[b]165	1.1[a]
IC 1459.....	CTIO 4m	4200	42	180	1.1[a]
.....	CTIO 4m	4200	42	165	1.1[a]
.....	CTIO 4m	5200	30	120	1.1[a]
.....	CTIO 4m	5200	30	[b]150	1.1[a]
.....	CTIO 4m	4200	[c]152	105	1.1[a]
.....	CTIO 4m	5200	[c]132	124	1.1[a]

Notes – [a]Early CTIO data with $\sigma_i \sim 110$km s^{-1}, and generally poorer S/N per unit time compared to later data. [b]S/N degraded by clouds and/or moon. [c]Minor axis. NGC 2768 KPNO 2.1m spectrum taken parallel to minor axis, but offset 10" W of nucleus. [d]Two separate wavelength regions processed separately from each plate (around 4200 Å and 5200 Å). [e]Position angle changes with radius. Col.(2) gives the observatory and telescope. The wavelength region is given in col.(3), and the position angle (defined as degrees E from N) in col.(4). The integration time is given in minutes in col.(5), and the slit width is given in arcsec in col.(6).

NGC 3557. Subsequent comparison of the data from the different position angles showed that the systematic differences, if any, were small compared to the random errors. The data were thus averaged to give mean profiles.

Furthermore, with the availability of higher quality surface photometry, it has become clear that the true major axis position angle differs from that used for some galaxies. The differences are not large. In fact, the mean difference is 4° with an rms dispersion per galaxy of 3°. The true position angles are given in Table 1, and can be compared with the actual position angles used in Table 3.

3. REDUCTION AND ANALYSIS

Photometric and geometric rectification of these data followed the now standard procedures for image intensifier/photographic spectra, as discussed, e.g., by Illingworth & Schechter (1982), Davies & Illingworth (1983), and Binney *et al.* (1990). In summary, the steps carried out were:

Digitization, using the KPNO PDS microdensitometer, of the long-slit and standard star spectra, full-slit HeNeAr arc line plates, and calibration plates. The PDS scans were made with a 25×25 μm aperture to ensure adequate sampling of the data. The output format of the long-slit galaxy spectra was 1024×512 pixels;

Transformation of the PDS density data (from its $0\leqslant D\leqslant5.115$ scale) onto a linear intensity scale;

Mapping the geometric distortion (along the dispersion direction) of the system using the full-slit HeNeAr arc spectra. The residual systematic deviations from the fitted polynomials were generally less than 10 km s^{-1}, and were uncorrelated from line to line. Thus, given adequate S/N, absorption line velocities could be measured to significantly <10 km s^{-1}. The S distortion was mapped by measuring the position $y(\lambda)$ of the galaxy nucleus on each spectrum;

Interpolation using splines to remove these distortions and to map the data onto a logarithmic grid in wavelength;

Normalization of the slit response function using a night-sky emission line. The flux in the emission line was measured across the spectrum, and a polynomial fitted giving a measure of the throughput of the system as a function of distance along the slit. The corrections applied through this "slit response function" were typically 10% to 20% from center to edge. The accuracy of this procedure was verified by checking the residuals in night sky lines other than the one(s) measured;

Generation of high S/N spectra of the night sky from the outer edges of the galaxy frames. Careful "cleaning" of the data to remove image intensifier ion events and photographic glitches was found to be necessary before the rows selected to give the sky spectrum were averaged. A median filter did not work well because it also removed the night-sky emission lines, and so "cleaning" was done using a mean-sigma rejection routine that was applied within a defined box whose location was set interactively;

Subtraction of the appropriate spectrum from each galaxy frame, verifying the accuracy using the frame blink capability of the KPNO image display system. This frame blink capability was found to be essential for ensuring that the sky subtraction was satisfactory.

The stellar spectra were processed in the same way, being finally reduced to a 1024×1 very high signal-to-noise row vector for subsequent use in the Fourier Quotient analysis.

3.1 Fourier Quotient Analysis

The velocity and velocity dispersion profiles were then derived using the Fourier Quotient technique as described by Schechter & Gunn (1979) and as used and tested by Illingworth & Schechter (1982), and Davies & Illingworth (1983). The usual steps were taken to ensure the integrity of the technique, i.e., (i) a cosine bell masking of the input spectrum, (ii) removal of the mean and of the low wave number components by fitting a low order polynomial (typically 3) through the data, (iii) linear interpolation across the strongest (and thus poorly subtracted) night sky emission lines, (iv) fitting over a range in wave number (typically $10<k<250$) that was found to be relatively insensitive to the exact values chosen, and (v) comparison of the results from several template stars which demonstrated that the results were independent of the choice of star.

The fit of the quotient of the galaxy and star Fourier transforms gives the radial velocity v_r, the stellar velocity dispersion σ, and a scale factor γ, along with error estimates for all three components from the simultaneous fit of the assumed Gaussian broadening profile. Experiments by Schechter & Gunn (1979) and Kormendy & Illingworth (1982) have shown that the Fourier Quotient technique tends to overestimate the velocity dispersion when σ becomes comparable to or falls below the instrumental resolution (typically $\sigma_i\approx80$ km s^{-1}, but $\sigma_i\approx110$ km s^{-1} for the early CTIO data), particularly when the S/N is low. It is clear that the degree to which the velocity dispersion is overestimated is a function of the signal-to-noise ratio and the spectral match between the template star and the galaxy, and is difficult to quantify. Only for NGC 4976 for which only one early CTIO plate was available is this effect potentially the source of any problems. The remaining galaxies should be unaffected. For example, there was no systematic difference between the early CTIO data for NGC 4697, and that obtained later at CTIO when the resolution had improved dramatically.

It has also been noted by Kormendy & Illingworth (1982) and Schechter & Gunn (1979) that the velocity dispersions derived from spectra containing strong and intrinsically broad spectral features, e.g., the H and K lines of Ca II (3934 and 3968 Å) are systematically overestimated. Thus, as in Kormendy and Illingworth, the velocity dispersions were derived from a region that excluded these features, while the velocity results included the full spectrum. In several cases data were available from both the 5200 and the 4200 Å regions, allowing comparison of the velocity dispersion profiles. The agreement was excellent. In fact, for NGC 4472, data were available from both CTIO and KPNO in both wavelength regions. The velocity

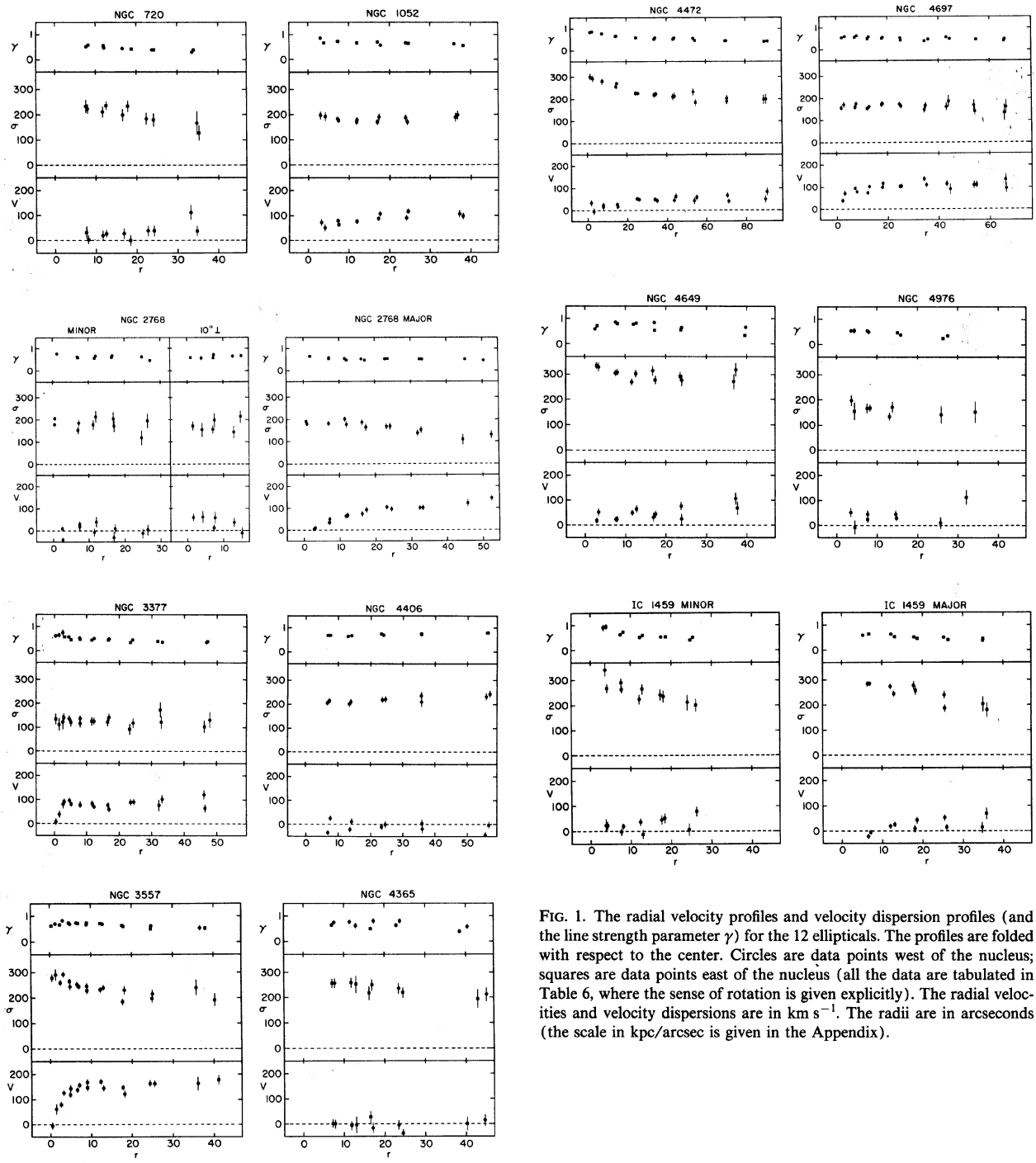

FIG. 1. The radial velocity profiles and velocity dispersion profiles (and the line strength parameter γ) for the 12 ellipticals. The profiles are folded with respect to the center. Circles are data points west of the nucleus; squares are data points east of the nucleus (all the data are tabulated in Table 6, where the sense of rotation is given explicitly). The radial velocities and velocity dispersions are in km s^{-1}. The radii are in arcseconds (the scale in kpc/arcsec is given in the Appendix).

dispersion profiles were very similar, and differed from the mean profile with an rms one-sigma deviation of only 6%.

The RCA C33063 image intensifier is subject to considerable internal light scattering, as are all such magnetically focused intesifiers, and so the resulting data frames typically contain an additive component due to scattered light. Of intensified systems only those employing photon event detection, as opposed to analog integration onto the final detector, will be substantially free of this problem. This background is not a strong function of the spatial characteristics of the illumination of the image intensifier; i.e., only very low spatial frequency components are present in the scattered light. Thus the scattered light should not affect the determination of the velocities and velocity dispersions. This has, in fact, been shown by Kormendy and Illingworth to be the case. However, the line strengths are strongly affected by this essentially indeterminate additive component. Thus the gradients in γ should not be interpreted as real gradients in line strength. In particular, these data cannot be used to determine radial variations in any of the absorption lines in these spectra.

3.2 Gaseous Component Velocities

Two of these galaxies have weak, but measurable, emission from [O II]λ3727 Å. They are NGC 2768 and IC 1459. The [O II] doublet was not resolved, at least in the inner regions, and so velocities were measured differentially about the nucleus. The positions of the emission lines were measured from the digitized data using an automated line tracking and fitting routine, and also directly from the plates using a Grant measuring engine. Similar results were obtained with both techniques. The measured [O II] velocities for NGC 2768 are given in Table 7 in the Appendix (and shown in Fig. 2). The results for IC 1459 are not given since the S/N was low compared to the measurements that were made and presented by Franx & Illingworth (1988).

The mean rotation was then taken to be half the peak-to-peak value at each radius. This approach eliminates any effect on the measured velocities of symmetric radial variations in the relative strengths of the two components due to changes in the electron density n_e. This may not be a concern, however, since the relative strengths of these components may not even change with radius. Davies & Illingworth (1986) noted that the significantly stronger [O II] emission in NGC 1052 arises from regions where n_e appears to be below the low density limit of $n_e < 300$ cm^{-3}, even in the nucleus (see, also, Minkowski & Osterbrock 1959). Under these circumstances the flux ratio in the doublet will not change with radius, and no systematic velocity shifts will occur.

3. KINEMATIC RESULTS

The velocity v_r, velocity dispersion σ and line strength γ results with error estimates from the fits are shown in Fig. 1 and tabulated in the Appendix in Table 6. The data have been folded about the nucleus as defined by the row of maximum intensity in the data, or by the symmetry point defined by the intensities at larger radii in the cases where the inner regions were photographically saturated. Most of our spectra were subject to saturation. In some cases, namely NGC 2768, 3377, 3557, 4472, and 4697, shorter integrations were taken to ensure that kinematic data could be obtained into the core.

The velocity dispersions agree well with other results. The mean difference (in the sense (*us-them/them*) for the five galaxies which have central measurements (those with σ measurements for $r < 3''$–$4''$ typically) that can be compared directly to the data of Davies *et al.* (1987) is -0.02 ± 0.03. A similar comparison with FIH between $\langle \sigma_{r_e/2} \rangle$ for the five galaxies in common yielded a mean difference (in the same sense) of -0.05 ± 0.05. The differences are encouragingly small. The rotational velocities agreed quite well also. The mean difference in the rotation was $0.2\sigma_v$ (from differencing the average velocities in Table 4 with those determined by FIH in their Table 4). The largest discrepancy was for NGC 4472, for which we chose a much larger mean radius to determine the $\langle v_{\rm rot} \rangle$. The measurements of FIH beyond 10″ agree well with those here, as does our $\langle v_{\rm rot} \rangle$ with the FIH $v_{\rm major}$ determined from the fitted model.

Dispersion and rotation profiles are available for a number of these galaxies from sources other than FIH and Davies *et al.* (1987). For example, dispersion and rotation profiles are given for NGC 720, 1052, and 4697 by Binney *et al.* (1990); the agreement is good for the dispersion and rotation profiles (and not unexpected since the same type of data, and similar analysis techniques, were used). NGC 4472 has also been studied by Davies & Birkinshaw (1988) and Saglia *et al.* (1993). The agreement between ourselves and these other measures in the velocity dispersion in the inner regions is excellent—within 5%. However, our velocity dispersion profile falls more rapidly and is about 20% lower than both at about 40″ where there is overlap in all three datasets. It is not clear why. Our data included four spectra, two from CTIO and two from KPNO, in two different spectral regions. The dispersions are internally consistent, though the scatter is large within any single data set. While some of the difference may be due to the quite low velocity resolution used by Davies and Birkinshaw, this was not the case with the Saglia *et al.* data. The rotational velocity profiles are consistent between all three groups (with $v_{\rm max} \sim 50$–60 km s^{-1} around 30–60 arcsec).

Bender (1988) has published data for two of the galaxies studied here. He also finds that the rotation on the major axis of NGC 4406 for $r > 10''$ is consistent with zero. For NGC 4365 he detects slight rotation of ~ 15 km s^{-1}, which is to be compared to our 5 ± 6 km s^{-1}, a less than 2σ difference (when the comparable uncertainty in his mean is included). The velocity dispersion profiles for both galaxies agree very well (to $\sim 5\%$). The dispersion derived by Jedrzejewski & Schechter (1989) for the minor axis of NGC 4406 also agrees very well with our major axis data.

Bertola *et al.* (1988) have measured the minor axis rotation and dispersion profile for NGC 4976. The mean velocity dispersion from their data (~ 160 km s^{-1}) agree well with our (major axis) $\langle \sigma_{r_e/2} \rangle$ of 162 km s^{-1}. The mean minor axis rotation that can be derived from Fig. 1(f) of Bertola *et al.* is consistent with zero; i.e., $v_{\rm rot} \sim 5 \pm 7$ km s^{-1}, in contrast to the major axis velocity of 34 ± 10 km s^{-1} found here.

With the single exception of the major axis profile of NGC 4472, the velocity dispersion results from many authors are remarkably consistent (as are the rotational velocities).

The kinematic properties of these galaxies are summarized in Tables 4 and 5. In Table 4 the (error weighted) mean rotational velocity is given with formal errors. As discussed in FIH, the systematic errors are likely to be dominant at the ~ 5 km s^{-1} level, and so this value is the minimum assigned, even though the weighted average sometimes gave formal errors < 5 km s^{-1}. The radial range from which this mean is derived is also given. FIH also fitted a simple analytic form to the rotation data and determined the velocity at 20 arcsec. Since this procedure gave results that were typically the same within the errors to the weighted average, only the latter mean values are tabulated here.

TABLE 4. Rotational velocities.

Galaxy (1)	Δr " (2)	$\langle r \rangle$ " (3)	$\langle v_{rot} \rangle$ km s^{-1} (4)
NGC 720	8 – 40	19	27± 8
NGC 1052	10 – 40	23	92± 5
NGC 2768	20 – 60	35	109± 6
[a]NGC 2768	5 – 30	16	13± 7
NGC 3377	5 – 50	21	82± 5
NGC 3557	5 – 50	16	152± 5
NGC 4365	7 – 50	21	5± 6
NGC 4406	5 – 60	28	8± 6
NGC 4472	20 – 90	53	51± 5
NGC 4649	10 – 40	23	55± 8
NGC 4697	10 – 70	36	101± 5
NGC 4976	5 – 40	17	34±10
IC 1459	10 – 40	23	28± 7
[a]IC 1459	8 – 30	16	26± 9

Notes – [a]Minor axis data. Col.(2) gives the radial interval in arcseconds over which the velocities are averaged. The mean radius is given in col.(3), and the mean rotational velocities for the major (and minor) axes are listed in col.(4) with their errors. The weighted means are given. The variances in the means were derived for both weighted and unweighted averages. The average of the uncertainties in the mean is that quoted. The sense of the rotation is given in the data table in the Appendix (Table 6).

Mean velocity dispersions were also derived. These are tabulated in Table 5. As has become customary (see, e.g., FIH or Davies *et al.* 1983), the mean dispersion within $r_e/2$ has been derived, using the r_e values listed in Table 1. The logarithmic gradient α of the velocity dispersion profile has also been determined for each of the galaxies, with formal errors of the fit. The dimensionless ratio $\langle v_{rot} \rangle / \langle \sigma_{r_e/2} \rangle$ of the mean rotation and the mean velocity dispersion has then been derived for each galaxy. Finally, the ratio which characterizes the degree of rotational support in terms of that expected for a rotationally flattened oblate spheroid, i.e., $(v/\sigma)^* = (\langle v_{rot} \rangle / \langle \sigma_{r_e/2} \rangle)/(v/\sigma)_{oblate}$ (see Davies *et al.* 1983) is tabulated in the last column of Table 5. NGC 3557 is consistent with being a rotationally flattened object. This is quite unusual for such a luminous elliptical.

TABLE 5. Velocity dispersions.

Galaxy (1)	$\langle \sigma_{r_e/2} \rangle$ (2)	α (3)	$\langle v_{rot} \rangle / \langle \sigma_{r_e/2} \rangle$ (4)	v/σ^* (5)
NGC 720	225 ± 6	-0.27 ± 0.08	0.12 ± 0.04	0.15 ± 0.05
NGC 1052	185 ± 5	-0.01 ± 0.02	0.50 ± 0.03	0.83 ± 0.05
NGC 2768	183 ± 5	-0.05 ± 0.02	0.60 ± 0.04	0.65 ± 0.04
[a]NGC 2768	188 ± 8	-0.03 ± 0.03	0.07 ± 0.04	... ± ...
NGC 3377	128 ± 5	-0.03 ± 0.03	0.64 ± 0.05	0.69 ± 0.05
NGC 3557	251 ± 8	-0.10 ± 0.02	0.61 ± 0.03	1.07 ± 0.05
NGC 4365	243 ± 5	-0.12 ± 0.03	0.02 ± 0.02	0.04 ± 0.04
NGC 4406	217 ± 5	0.06 ± 0.02	0.04 ± 0.04	0.07 ± 0.07
NGC 4472	252 ± 9	-0.14 ± 0.02	0.20 ± 0.02	0.44 ± 0.04
NGC 4649	302 ± 7	-0.07 ± 0.02	0.18 ± 0.03	0.39 ± 0.07
NGC 4697	163 ± 5	-0.00 ± 0.02	0.62 ± 0.06	0.82 ± 0.08
NGC 4976	162 ± 8	-0.15 ± 0.06	0.21 ± 0.09	0.32 ± 0.14
IC 1459	275 ± 8	-0.20 ± 0.05	0.10 ± 0.03	0.17 ± 0.05
[a]IC 1459	270 ± 13	-0.19 ± 0.05	0.10 ± 0.04	... ± ...

Notes –[a]Minor axis data. The mean velocity dispersion along the major (and minor axis) out to $r_e/2$ is given in col.(2) in km s^{-1}. The data points were not weighted by their errors. Central values from Davies *et al.* (1987 – see Table 1) are also included in the mean. Col.(3) gives the index α from a power law fit ($\sigma = \sigma_c r^{\alpha}$) to the velocity dispersion profile. The formal errors from the fit are given. Col.(4) gives the usual dimensionless ratio that is used to characterize the rotational flattening. Col. (5) is the ratio of the observed value in (4) with that expected for a rotationally flattened oblate spheroid (as, e.g., in Davies *et al.* 1983).

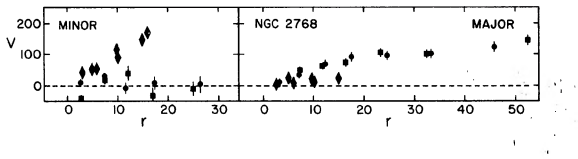

FIG. 2. The emission line rotation data for NGC 2768 from Table 7. The [O II] λ3727 Å velocities are shown as the filled diamonds, superimposed on the stellar rotation velocities (filled circles and squares) from Fig. 1. The velocities are in km s^{-1}, and the radii are in arcsec from the nucleus (where 1"=0.13 kpc for H_0=50 km s^{-1} Mpc^{-1}). The height of the diamonds is indicative of the typical measurement errors for the emission lines (i.e., ±20–30 km s^{-1}).

4. DISCUSSION

While the detector combination used here does not have the QE of more recent observations that used CCDs, the long integration times necessitated by the use of photographic plates as the final detector has resulted in quite high S/N for much of these data. Thus the profiles in several cases (e.g., NGC 2768, NGC 3377, NGC 4472, and NGC 4697) extend to large radii. However, the profiles for any of the galaxies typically do not extend beyond $1r_e$; a variety of factors make it very difficult to obtain results much beyond r_e, through it is primarily due to the difficulty of doing adequate sky subtraction.

Several points can be made from these data.

Rotational properties: The well known range in rotational properties among ellipticals is made strikingly apparent by comparing the results for NGC 3557 and NGC 4365 in Fig. 1. Both are luminous E3 galaxies with similar velocity dispersions, yet NGC 3557 shows over 150 km s^{-1} of rotation on the major axis, while the major axis rotation $\langle v_{rot} \rangle$ for NGC 4365 is consistent with being zero (formally 5±6 km s^{-1}). However, as FIH noted, only a very small fraction of ellipticals appear to show no rotation whatsoever. The two galaxies (NGC 4365 and NGC 4406) here that are consistent with having zero rotation on the major axis actually have been found to be minor axis rotators (Wagner *et al.* 1988; FIH) with average minor axis velocities of 40–50 km s^{-1}. NGC 3557 is dynamically a "classical" elliptical in that it is consistent with being an isotropic-dispersion, rotationally-flattened oblate spheroid [though there is no guarantee that it has such a structure!—see Franx *et al.* (1991)]. There is no evidence that NGC 3557 is other than a *bona fide* elliptical galaxy.

Rotation curve shape: The uniformity of the shape of the rotation curve in these and other published data is noteworthy. Normalized rotation curves are shown in Fig. 3 for several galaxies (all those in the sample with $\langle v_{rot} \rangle \geqslant 80$ km s^{-1}—the v_{max} used for normalization was 101 km s^{-1} for NGC 1052, 133 km s^{-1} for NGC 2768, 90 km s^{-1} for NGC 3377, 156 km s^{-1} for NGC 3557, and 111 km s^{-1} for NGC 4697—the data for NGC 4472 shows similar behavior, as can be seen in Fig. 1, but was not included because of the large scatter that results from the small amplitude of its rotation curve). Where the S/N is adequate to allow the shape of the rotation curve to be characterized, it is clear that, in most cases, the rotational velocity rises

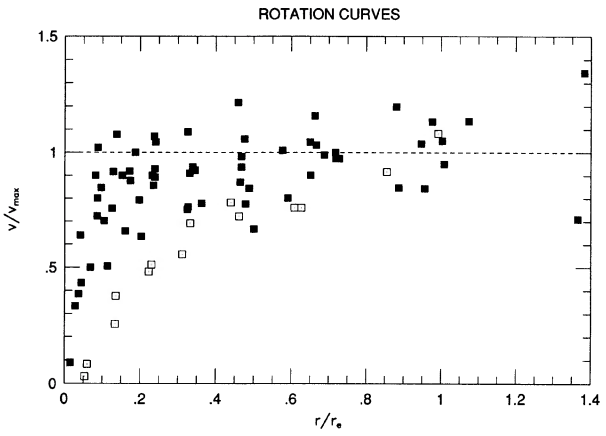

FIG. 3. Normalized rotation curves for the five ellipticals in this sample that have maximum rotational velocities $\langle v \rangle$ that are greater than 80 km s^{-1}. The majority of these ellipticals have rotation curves that rise quickly (within $r/r_e < 0.1$–0.3) to their asymptotic value; NGC 2768 (shown as the open squares) is the exception. It's rotation curve rises slowly and never appears to flatten.

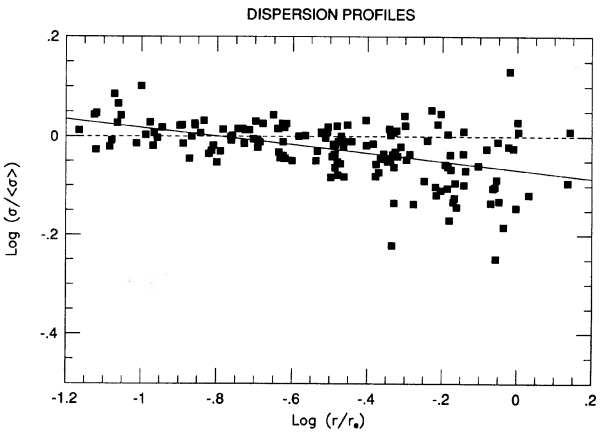

FIG. 4. Velocity dispersion profiles for the elliptical galaxies in this paper. They are normalized by the mean dispersion within $r_e/2$, as given in Table 5 (thus $\langle \sigma \rangle \equiv \langle \sigma_{r_e/2} \rangle$), and by the effective radius r_e given in Table 1. Error bars are not plotted since the scatter is indicative of the typical uncertainty. The mean gradient is very small from $\sim 0.1 r_e$ to r_e. The line corresponds to the mean logarithmic gradient determined for this sample; i.e., $\langle \alpha \rangle = -0.09$.

quickly to a certain value, changing little thereafter. NGC 2768 is the only clear example in this sample where the rotational velocity appears to continue rising beyond a few tenths of r_e. The rise to the "flat" portion typically occurs within a small fraction of r_e; in fact, usually within $0.2 r_e$, and sometimes even less ($< 0.1 r_e$). Yet is interesting to note that, energetically, the rotation is usually insignificant. So, unlike the case in disk galaxies where the "flat" rotation curves derive their characteristic shape from the mass distribution, the "flat" rotation profiles must result from an interesting relationship between the specific angular momentum and the energy.

Velocity dispersion profiles: While the observed velocity dispersion profiles are but the projection of the line-of-sight components of the stellar velocity dispersion tensor and cannot be unambiguously interpreted to give mass distributions and hence $\mathcal{M}/L$ profiles, they are of particular interest if the mass distribution can be determined in other ways (e.g., gas rotation, x-ray halos, shells, etc.). Under these circumstances, the form of the velocity dispersion profile can be used to study the anisotropy in the velocity distribution. Even without independent estimates of the mass distribution, the velocity dispersion profiles can be of value in discussions of the dynamics and of the $\mathcal{M}/L(r)$ profiles (see, e.g., Davies & Illingworth 1983; Tonry 1983; Saglia *et al.* 1993). The difficulty of extending these profiles beyond $\sim r_e$ should not be underestimated, however.

All the logarithmic gradients were negative or consistent with 0, i.e., with no change in the velocity dispersion with radius out to radii $r \sim r_e$. Even the largest slope is small; the largest power law index is -0.27 for NGC 720. The mean of all the major axis logarithmic gradients is $\langle \alpha \rangle = -0.09$. The mean gradient for the data of FIH is -0.06. The uncertainty in these means is typically ± 0.02 to ± 0.03. The velocity dispersion changes very little with radius; a gradient $\alpha = 0.08$ corresponds to only a 20% decrease in σ for an order-of-magnitude change in radius.

The profiles are displayed in dimensionless form in Fig. 4. The normalizations are r_e from Table 1, and the mean dispersion within one-half r_e, i.e., $\langle \sigma_{r_e/2} \rangle$, from Table 5. The very small gradient over the range $\sim 0.1 r_e$ to $\sim r_e$ is clearly seen.

Minor axis rotation: Minor axis rotation and dispersion profiles were also measured for two elliptical galaxies, the E5–6 galaxy NGC 2768 and the E3 galaxy IC 1459. There was a very marginal 2σ detection of rotation on the minor axis of IC 1459, but this could have resulted from one of the "minor axis" position angles that did not correspond closely to the mean position angle of the minor axis (the position angle of the axis shifts by $> 15°$). No minor axis rotation was detected by FIH. The striking, kinematically distinct core of IC 1459 was not detected in these data because the central regions were saturated. IC 1459 has been discussed in some detail by Franx & Illingworth (1988) and FIH, and will not be discussed further.

The minor axis of NGC 2768 shows little, if any, rotation at 13 ± 8 km s^{-1}. NGC 2768 shows a very small change of position angle with radius [$\Delta\Theta < 5°$; Peletier *et al.* (1990)], and so the minor axis position angle is quite well defined at $5° \pm 1°$ (Peletier *et al.* give the major axis PA as $95° \pm 1°$ over the radius range appropriate for the kinematic data). Using the definitions of FIH for the kinetmatic angle, where $\hat{\Theta}_{\rm obs,min}$ is the actual slit position angle used for the minor axis observations,

$$|\tan(\hat{\Pi} - \hat{\Theta}_{\rm obs,min})| = \left|\frac{v_{\rm minor}}{v_{\rm major}}\right| \qquad (1)$$

with $|v_{\rm minor}/v_{\rm major}| = 0.13 \pm 0.08$ from Table 4 gives $\hat{\Pi} - \hat{\Theta}_{\rm obs,min} = 7° \pm 4°$, or $\hat{\Pi} = 7° \pm 4°$ (since $\hat{\Theta}_{\rm obs,min} = 0°$ (Table 3); also note that the angle $\hat{\Pi}$ is chosen such that the maximum radial velocity occurs near $\hat{\Pi} - 90°$). Broadly, $\hat{\Pi}$ can be taken to be the position angle of the rotation axis

(exactly so for a disk with circular streaming or for figure rotation). The kinematic misalignment angle

$$\hat{\Psi}=\hat{\Pi}-\hat{\Theta}_{\min}, \quad (2)$$

is simply the difference between the "rotation" axis $\hat{\Pi}$ and the photometric axis $\hat{\Theta}_{\min}$. For NGC 2768 where $\hat{\Theta}_{\min}$ is $5°\pm1°$, $\hat{\Psi}=2°\pm4°$. Thus the rotation axis appears to be very closely aligned with the photometric (minor) axis.

Velocity field: Modeling of the form of the velocity field in elliptical galaxies has lagged the comprehensive studies of the bulges of disk galaxies (e.g., Kormendy & Illingworth 1982; Jarvis & Freeman 1985). While a number of early dynamical studies were made [e.g., the pioneering effort of Satoh (1980)], a rather detailed dynamical modeling of galaxies with velocity and velocity dispersion maps have been done only recently (Binney *et al.* 1990; van der Marel *et al.* 1990). van der Marel (1991) has extended this modeling to a larger sample.

Some additional data useful for velocity mapping has been obtained in this project on a more flattened galaxy, the E6 elliptical NGC 2768. Its mean ellipticity is 0.47, but the flattening changes from $\epsilon\sim0.3$ to $\epsilon\sim0.6$ over a radial range of 10″–150″. Data are presented here for NGC 2768 in Fig. 1 (the 10 arcsec "perpendicular profile"—a spectrum offset from the nucleus by 10 arcsec along the major axis, but with the slit parallel to the minor axis). While quite limited data, the rotational velocity v_z profile clearly falls to low values of rotation (i.e., to the systematic velocity) quite rapidly with z (at $z\approx12''$–$15''$, or by $<r_e(major)/4$). The velocity zero-point was derived, as in previous studies (e.g., Kormendy & Illingworth 1982), by matching the $z=0$ velocity data from the perpendicular profile to the major axis rotation curve at the radius of the cut (10″). Binney *et al.* (1990) noted that the change in v_z was too rapid for their models of NGC 4697; NGC 2768 is probably like NGC 4697.

The bulge studies (e.g., Kormendy & Illingworth 1982) clearly establish the existence of two apparently distinct forms for the velocity field, namely the "spheroidal" form that occurs in normal bulges and the "cylindrical" form that occurs in box- and peanut-shaped bulges. Observationally, the distinction lies in that the rotational velocity decreases with z distance from the equatorial plane in the former case, whereas the velocity remains constant, apparently to many scale heights, with height z in the cylindrical case. NGC 2768 seems to be like other ellipticals in that the velocity field is of the "spheroidal" form.

Gaseous component rotation: The existence of weak but measurable extended [O II] emission in the two ellipticals, NGC 2768 and IC 1459 is valuable. The circular velocity and direction of the rotation axis of the gas are both extremely useful parameters that can, in principle (with data of high S/N), be derived from mapping the extended line emission. The velocities for the gas in IC 1459 have been discussed by Franx & Illingworth (1988). The data here do not extend to large radii, but confirm the velocities seen by them and that the emission is largely confined to the major axis. The sense of rotation of the gas is the same as that of the stellar component (at radii $r>10''$).

In the case of NGC 2768, the [O II] emission is more extensive and of higher surface brightness, allowing greater mapping to be carried out. The emission line velocities are shown in Fig. 2, and are tabulated in Table 7 in the Appendix. Large rotation velocities are seen on the minor axis (to ~160 km s^{-1}; redshifted to the north), while those on the major axis are quite small (only ~20 km s^{-1}; redshifted on the western side of the galaxy). Emission is also seen on the spectrum parallel to the minor axis (i.e., set to PA 0°), but offset 10″ west of the nucleus. The gas is obviously rotating, but the line is much weaker and not measurable with any reasonable accuracy.

The sense and the amplitude of the gas rotation is consistent with the results of Kim (1989) who measured about 140 km s^{-1} of rotation on the minor axis in PA 0° from Hα/[N II]. The sense of the rotation on the major axis is opposite that of the stars. Bertola *et al.* (1992) found such a difference (but in the opposite sense), but measured slightly larger rotational velocities on the major axis ($\sim$30–40 km s^{-1}). The nearly linear rise seen on the minor axis is most likely due to the small offset in the position of the slit from the nucleus. The slit was located parallel to the minor axis but offset by about 4″ to the east. The net effect of such a shift will be to decrease the rate at which the rotation curve rises. More comprehensive data are given by Fried *et al.* (1994).

The data shown here, combined with that of Kim, and that of Bertola *et al.*, show that the rotation axis of this gaseous component is essentially perpendicular to that of the stellar component. NGC 2768 has a polar orbiting gas disk. The net, small counter-rotation seen on the major axis here and by Bertola *et al.* (1992) indicates that the gas disk is probably slightly inclined to the minor axis. This polar disk is, however, small in extent compared to the gas disks that surround the S0 galaxies that have been studied by Whitmore *et al.* (1987, and references therein). As for other cases of components that have dramatically different angular momenta (in orientation), these data also suggest an external origin for the gaseous material in the polar gas disk/ring. The polar gas is discussed in more detail in Fried *et al.* (1994).

5. SUMMARY

Long slit spectra have been obtained of a sample of nearby elliptical galaxies. The dispersion and rotation profiles typically extend to radii comparable to r_e, larger than has usually been the case for other samples in recent years. The very low slopes to the dispersion profiles (as characterized by their logarithmic gradients) and the degree to which the rotation curves are "flat" (even though the rotaion is energetically insignificant in essentially all cases) are interesting features of these data. A polar orbiting gas disk has also been found in NGC 2768, and is another example of the utility of the gas distribution and kinematics for elucidating the evolutionary history of ellipticals. The kinematic results on these 12 ellipticals add to the growing database of dispersion and rotational profiles that is required for elucidation of the properties of ellipticals.

TABLE 6. Rotation and dispersion results.

r	v_r	Δv_r	σ	$\Delta\sigma$
"	km s^{-1}		km s^{-1}	
NGC 720 PA 142 Major Axis				
35.0	37	20	127	30
24.2	38	21	178	26
18.2	-1	20	233	22
12.5	26	15	235	16
7.7	32	23	232	26
-8.1	-3	17	222	18
-11.7	-21	19	210	21
-16.8	-27	20	198	24
-22.6	-38	20	183	23
-34.0	-111	29	165	46
NGC 1052 PA 118 Major Axis				
37.3	96	13	189	17
24.5	117	9	170	11
17.2	88	8	170	10
12.0	76	8	170	9
7.5	64	6	176	8
4.2	51	13	193	17
-3.2	-73	13	197	15
-7.3	-80	6	183	7
-12.1	-77	8	178	9
-17.6	-107	9	190	12
-24.1	-91	10	187	13
-37.1	-106	13	198	17
NGC 2768 PA 90 Major Axis				
52.6	-144	12	131	16
32.2	-101	10	139	13
23.3	-104	10	169	12
16.5	-74	11	187	13
11.8	-64	10	202	11
7.2	-50	8	183	9
2.8	-4	8	....	....
1.1	....	....	180	6
-0.9	....	....	193	6
-3.2	11	9	....	....
-7.1	34	8	187	9
-12.2	68	12	178	13
-17.6	92	13	165	15
-24.5	96	12	170	14
-33.2	101	12	153	15
-45.3	122	17	110	24
NGC 2768 PA 0 Offset 10" West				
15.2	12	25	213	27
7.4	-11	15	155	19
1.7	-59	17	171	20
-4.3	-61	26	154	32
-7.8	-57	28	197	31
-13.1	-36	20	143	28
NGC 2768 PA 0 Minor Axis				
26.5	4	24	196	32
17.3	9	21	171	26
11.4	-7	18	178	22
7.3	30	12	153	15
2.5	9	10	....	....
0.7	....	....	206	6
-0.6	....	....	179	6
-2.7	41	12	....	....
-7.4	-18	12	186	14
-12.1	-39	22	214	26
-17.0	31	27	205	31
-25.0	11	22	119	32
NGC 3377 PA 35 Major Axis				
46.4	64	16	103	25
32.5	76	23	173	30
23.4	89	13	92	22
16.6	76	12	122	16
11.7	83	12	125	16
7.9	81	11	116	17
5.2	81	9	120	15
3.0	92	11	141	17
0.5	8	12	135	22
-1.5	-39	14	112	26
-2.8	-81	17	122	29
-4.7	-97	8	136	12
-8.0	-77	8	136	11
-12.3	-70	9	125	13
-17.0	-60	12	141	16
-24.4	-90	12	118	19
-33.2	-102	17	121	25
-47.0	-121	19	131	32
NGC 3557 PA 35 Major Axis				
40.8	177	19	191	25
24.7	163	12	197	17
17.8	146	10	184	12
12.4	170	9	231	10
9.1	145	10	227	11
7.1	156	9	243	9
4.8	118	10	264	10
2.6	78	11	258	11
0.5	-6	14	277	15
-1.4	-60	20	290	22
-3.3	-125	10	292	10
-4.9	-143	12	243	13
-6.6	-137	9	252	10
-9.0	-167	11	245	12
-13.1	-144	9	239	10
-18.2	-121	14	229	17
-25.3	-161	13	215	16
-36.0	-162	26	239	31
NGC 4365 PA 39 Major Axis				
41.1	0	27	194	36
24.6	-38	16	219	19
16.5	27	22	217	25
13.1	-4	32	252	33
7.3	2	15	256	17
-7.9	1	17	256	18
-11.9	7	17	258	19
-17.1	17	20	248	21
-23.5	5	18	235	20
-44.9	-14	22	212	26
NGC 4406 PA 130 Major Axis				
56.9	-3	14	241	14
35.9	4	17	234	16
23.7	-10	11	217	12
13.7	-21	11	200	12
6.9	-35	9	204	10
-7.6	-26	9	213	10
-14.1	-12	12	208	12
-24.7	0	13	218	14
-36.0	19	18	208	19
-55.8	44	13	230	20
NGC 4472 PA 156 Major Axis				
89.6	-49	17	198	20
70.6	-66	11	189	14
53.7	-43	13	232	15
43.6	-45	12	209	13
35.1	-43	9	222	10
26.0	-49	7	225	7
15.2	-17	6	271	6
7.9	-24	10	281	11
1.8	-34	13	301	13
-3.1	-4	14	293	14
-7.8	15	10	278	10
-14.9	28	6	256	6
-24.8	53	8	227	9
-34.0	49	9	218	10
-44.4	63	12	213	14
-55.0	58	13	184	16
-71.0	39	11	203	13
-90.6	82	17	199	21
NGC 4649 PA 96 Major Axis				
37.4	69	26	271	29
23.9	77	15	291	17
17.5	44	14	276	16
12.7	65	13	301	14
8.0	25	10	307	12
2.9	18	11	334	13
-3.4	-52	14	328	17
-7.6	-23	10	304	11
-11.7	-49	11	268	12
-16.9	-31	17	313	19
-23.7	-25	20	275	22
-37.2	-107	23	318	25
NGC 4697 PA 62 Major Axis				
66.0	133	24	133	37
54.6	108	14	139	19
43.2	112	13	160	17
34.4	135	10	146	15
25.4	104	9	163	11
17.9	99	9	170	11
12.1	73	6	152	8
7.3	94	7	158	10
2.1	37	9	155	11
-3.1	-71	10	169	12
-7.9	-78	6	174	8
-12.9	-102	6	160	8
-18.1	-116	8	173	10
-24.8	-101	7	171	9
-35.1	-109	10	166	13
-44.3	-89	22	184	26
-53.9	-108	16	167	21
-66.5	-94	22	159	31
NGC 4976 PA 165 Major Axis				
33.1	112	28	153	40
13.8	29	10	134	15
7.4	23	11	168	14
4.3	-8	27	155	34
-3.4	-51	17	197	20
-7.5	-44	15	167	18
-14.1	-44	15	171	20
-25.7	-10	21	142	34
IC 1459 PA 35 Major Axis				
34.8	-14	21	203	29
25.4	-53	12	239	14
17.9	-9	14	277	15
12.0	-19	9	273	10
6.4	22	9	284	9
-7.0	-4	7	285	7
-12.9	26	10	244	11
-18.4	43	13	256	16
-25.7	15	11	186	14
-35.8	69	23	180	28
IC 1459 PA 142 Minor Axis				
24.3	-6	24	210	29
17.6	-45	18	240	22
12.4	-37	14	223	17
7.8	3	14	290	15
3.9	-23	25	341	24
-4.3	23	16	268	18
-8.0	20	11	263	13
-13.0	-12	17	264	19
-18.3	52	19	234	23
-26.3	78	18	199	25

Many of the issues that remain to be resolved for ellipticals are ones that require statistically significant samples.

The authors appreciate the many at KPNO and CTIO who ably and willingly assisted with the acquisition of these data and their analysis. We are grateful to many colleagues for stimulating discussion on these topics over the years, particularly James Binney, Harvey Butcher, Roger Davies, George Lake, Colin Norman, Doug Richstone, Paul Schechter, and Mark Whittle. J.F. would like to thank the Director of KPNO for the opportunity to work at the observatory during the course of the analysis of these data. J.F. is also particularly grateful for a fellowship from the Max-Planck-Institute for support during his visit to Kitt Peak.

APPENDIX: KINEMATIC DATA

The rotational velocity v_r and velocity dispersion σ are tabulated in Table 6 for the 12 galaxies studied here. The slit position angle (PA—defined east from north from 0° to 180°) is also indicated in the title line, as is the alignment with either the major or minor axis of the galaxy. Errors Δr_v and $\Delta\sigma$ are also tabulated. All velocities are referenced to the systemic velocity and are in km s^{-1}. All radii are in arcseconds, with *negative* radii for data in the *eastern* sector (E of the N–S line). The sense of the rotation can be established since redshifted velocities are positive with respect to the systemic velocity.

These results are the average of data from several plates in many cases, including averages from the two different wavelength regions used. Mean PAs are given for averages involving spectra at two slightly different PAs. No significant systematic differences were seen. As noted in the text, for the blue region spectra, velocities were derived from spectral regions that included the H and K lines of Ca II, whereas the velocity dispersions were measured from regions that excluded these features. The line strength γ is not tabulated as it is of little quantitative value (however, it is plotted in Fig. 1 along with the kinematic results).

TABLE 7. [O II] emission velocities.

$\lvert r\rvert$	v_r	Δv_r
"	km s^{-1}	
	NGC 2768 PA 90 Major Axis	
3.....	4	10
[g]5.....	24	20
6.....	7	15
[g]10.....	19	20
10.....	16	15
15.....	23	20
	NGC 2768 PA 0 Minor Axis	
3.....	43	10
[g]5.....	50	20
6.....	51	15
[g]10.....	112	20
10.....	88	15
[g]15.....	147	25
16.....	170	20

Notes—[g]Velocities derived from original plates with measuring engine. Remaining velocities derived from mapping of lines on digitized spectra. Errors estimated typically to be in range 10–20 km s^{-1} for these measurements. Lines measured differentially. Gas is redshifted on western end on major axis and on northern side on minor axis. Minor axis spectrum offset from nucleus by ~4" to the east.

The scales for the individual galaxies corresponding to $H_0=50$ km s^{-1} Mpc^{-1} and the group velocities v_{grp} (from Table 1) are as follows (all in kpc/arcsec): 0.10 for the "Virgo" objects (NGC 4365; 4406, 4472, 4649, 4697); 0.17 for 720; 0.13 for 1052 and 2768; 0.065 for 3377; 0.27 for 3557; 0.11 for 4976; and 0.16 for IC 1459.

Rotation velocity data are also tabulated for the extended [O II] emission in NGC 2768 in Table 7. Since peak-to-peak measures were made (see Sec. 2), the data are tabulated as a function of absolute radius. However, the sense of rotation was determined, and is noted in the table. While the major axis velocity measures are not tabulated for IC 1459 (see, instead, Franx & Illingworth 1988), the sense of rotation of the gas is the same as that of the stellar component (at radii $r>10$").

REFERENCES

Bender, R. 1988, A&A, 202, L5
Bertola, F., Capaccioli, M., Galletta, G., & Rampazzo, R. 1988, A&A 192,
Bertola, F., Buson, L. M., & Zeilinger, W. W. 1992, ApJ, 401, L79
Binney, J. J. 1978, MNRAS, 183, 779
Binney, J. J., Davies, R. L., & Illingworth, G. D. 1990, ApJ, 361, 78
Birkinshaw, M., & Davies, R. L. 1985, ApJ, 291, 32
Burstein, D., Davies, R. L., Dressler, A., Faber, S. M., Stone, R. P. S., Lynden-Bel, D., Terlevich, R., & Wegner, G. 1987, ApJS, 64, 601
Canizares, C. R., Fabbiano, G., & Trinchieri, G. 1987, ApJ, 312, 503
Davies, R. L., & Illingworth, G. D. 1983, ApJ, 266, 516
Davies, R. L., Efstatiou, G., Fall, S. M., Illingworth, G. D., & Schechter, P. L. 1983, ApJ, 266, 41
Davies, R. L., & Illingworth, G. D. 1986, ApJ, 302, 234
Davies, R. L., Burstein, D., Dressler, A., Faber, S. M., Lynden-Bell, D., Terlevitch, R. J. & Wegner, G. 1987, ApJS, 64, 581
Davies, R. L., & Birkinshaw, M. 1988, ApJS, 68, 409
Davies, L. E., Cawson, M., Davies, R. L., & Illingworth, G. 1985, AJ, 90, 169
de Vaucouleurs, G., de Vaucouleurs, A., Corwin, H. G. 1976, Second Reference Catalogue of Bright Galaxies (University of Texas Monographs in Astronomy No. 2, Austin) (RC2)
de Zeeuw, P. T., 1987, in Structure and Dynamics of Elliptical Galaxies, IAU Symposium 127, edited by T. de Zeeuw (Reidel, Dordrecht), p. 271
Disney, M. J., & Wall, J. V. 1977, MNRAS 179, 235
Djorgovski, S. 1985, Ph.D. thesis, Berkeley
Dressel, L. L., & Condon, J. J. 1978, ApJS, 36, 53
Fabbiano, G., Gioia, I. M., & Trinchieri, G. 1989, ApJ, 347, 127
Franx, M., & Illingworth, G. D. 1988, ApJ, 327, L55
Franx, M., Illingworth, G. D., & Heckman, T. M. 1989a, AJ, 98, 538
Franx, M., Illingworth, G. D., Heckman, T. M. 1989b, ApJ, 344, 613 (FIH)
Franx, M., Illingworth, G. D., & de Zeeuw, P. T. 1991, ApJ, 383, 112
Gerhard, O. E. & Vietri, M. 1986, MNRAS, 223, 377
Illingworth, G., 1981, in The Structure and Evolution of Normal Galaxies, edited by S. M. Fall, and D. Lynden-Bell (Cambridge University Press, Cambridge), p. 27

Illingworth, G. & Schechter, P. L. 1982, ApJ, 256, 481
Jarvis, B. J., & Freeman, K. C. 1985, ApJ, 295, 324
Jedrzejewski, R. I. 1987, MNRAS, 226, 747
Jedrzejewski, R., & Schechter, P. L. 1989, AJ, 98, 147
Kim, D-W. 1989, ApJ, 346, 653
Kormendy, J., & Illingworth, G. 1982, ApJ, 256, 460
Lauer, T. R. 1985, ApJS, 57, 473
Minkowski, R., & Osterbrock, D. 1959, ApJ 129, 583
Peletier, R. F., Davies, R. L., Illingworth, G. D., Davies, L. E., & Cawson, M. C. 1990 AJ, 100, 1091
Saglia, R. P., *et al.* 1993, ApJ, 403, 567
Sandage, A., & Tammann, G. A. 1981, A Revised Shapley Ames Catalogue of Bright Galaxies (Carnegie Institution of Washington, Washington, DC) (RSA)
Satoh, C. 1980 PASJ, 32, 41
Schechter, P. L., & Gunn, J. 1979, ApJ, 229, 472
Tonry, J. L. 1983, ApJ, 266, 58
van der Marel, R. P. 1991, MNRAS, 253, 710
van der Marel, R. P., Binney, J., & Davies, R. L. 1990, MNRAS, 245, 582
Wagner, S. J., Bender, R., & Möllenhof, C. 1988, A&A, 195, L5
Whitmore, B. C., McElroy, D. B., & Schweizer, F. 1987, ApJ, 314, 439
Wrobel, J. M., & Heeschen, D. S. 1984, ApJ, 287, 41